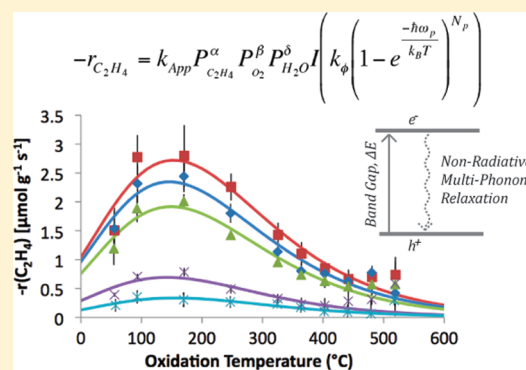


High-Temperature Photocatalytic Ethylene Oxidation over TiO₂Thomas A. Westrich,^{*,†} Kevin A. Dahlberg,[†] Massoud Kaviany,^{‡,§} and Johannes W. Schwank[†][†]Department of Chemical Engineering and [‡]Department of Mechanical Engineering, University of Michigan, Ann Arbor, Michigan 48109, United States[§]Division of Advanced Nuclear Engineering, Pohang University of Science and Technology, Pohang, Gyungbuk, 790-784, Korea

Supporting Information

ABSTRACT: Photocatalytic oxidation of ethylene was conducted in a novel two-dimensional packed bed reactor at higher temperatures (60 °C < *T* < 520 °C) than previously reported. Degussa P25 TiO₂ was used as a photocatalyst; samples of this TiO₂ were heat treated to different temperatures to obtain different phase compositions, surface areas, and surface hydroxyl concentrations. Maximum photocatalytic ethylene oxidation rates were observed between 100 and 200 °C. Further, oxidation rates greater than 75% of the maximum oxidation rate were observed over a large temperature range: 60 °C < *T* < 300 °C. At higher temperatures (*T* > 300 °C), decreasing oxidation rates were attributed to the nonradiative, multiphonon recombination of photogenerated charge carriers. Regression analysis of a nonlinear, multiphonon recombination model and a simplified chemical rate law were used to determine apparent reaction rate law parameters for the photocatalytic oxidation of ethylene and recombination parameters for the TiO₂ photocatalyst. Insights for the development and operation of novel high-temperature photocatalysts are also discussed.



INTRODUCTION

The necessity to find a more efficient TiO₂ photocatalyst has driven the investigation of the photocatalytic behavior of mixed phase TiO₂ photocatalyst, Degussa P25. This commercially available TiO₂ exhibits excellent photocatalytic activity compared to other TiO₂ photocatalysts. Possible reasons for enhanced photocatalytic activity include: surface area, crystalline phase composition, surface hydroxyl concentration, and interfacial charge transfer dynamics.^{1–7} Many of these characteristics are confounded with each other and the photocatalyst's heat treatment temperature. Prevailing hypotheses for enhanced photocatalytic activity of P25 surround the electronic states (location of the conduction and valence bands) of anatase and rutile TiO₂ phases in contact with each other in the photocatalyst, and charge transfer mechanisms that effectively separate charge carriers.^{8–11}

Charge carriers are produced when a photocatalyst absorbs a photon with sufficient energy: a valence electron is promoted to the conduction band, leaving a hole in the valence band. Recombination of these charge carriers is a major contributor to the inefficiency of photocatalysts.^{12–17} Finding a way to increase the charge carrier lifetimes would be important, as it would lead to the increased availability of reactive electrons and holes on the surface of the catalyst, which in turn would increase photocatalytic efficiencies. Increasing the carrier lifetime can be achieved very simply with the addition of metals, usually through photo-reduction of metal salts over the photocatalyst, or via simple metal impregnation methods.^{13,14,17,18} Other methods for increasing photocatalyst efficiencies rely on the optimization of electron and hole mobility, which increases the time the charge

carrier spends on the photocatalyst surface, rather than in the bulk photocatalyst.^{8,12–14,19,20}

In TiO₂-based photocatalytic oxidation mechanisms, such as photocatalytic remediation of volatile organic compounds (VOCs), the species primarily responsible for oxidation chemistry is the photogenerated hole.^{12,18,21–23} Photogenerated electrons migrate to regions in the catalyst with Fermi energy lower than that of the semiconductor, such as a metal (Au or Pt), while the holes migrate to photocatalyst defects and surface vacancies.²⁰ At the surface of the photocatalyst, the photogenerated hole is free to oxidize an adsorbed species, such as molecular oxygen, a surface hydroxyl, or adsorbed water molecule to produce O₂-superoxide, or hydroxyl radical; both species are responsible for the decomposition of adsorbed hydrocarbons into mineral acids and CO₂.^{6,12,13,15,21,23,22}

As photocatalytic oxidation reactions are generally thought to be nonactivated processes,^{12,24,25} they should be temperature independent. However, oxidation temperature influences photocatalytic oxidation rates for several VOCs due to changes in adsorption energy of polar and nonpolar reactants (e.g., water and ethylene).^{12,15,25–27} Analysis of experimental ethylene photocatalytic oxidation rates, for example, reveals an apparent activation energy of approximately 12.13 kJ/mol.^{25,28,29} Multiple studies have observed maximum rates of photocatalytic ethylene oxidation between 50 and 110 °C.^{25,28–31} However, these investigations do

Received: May 11, 2011

Revised: June 11, 2011

Published: June 19, 2011

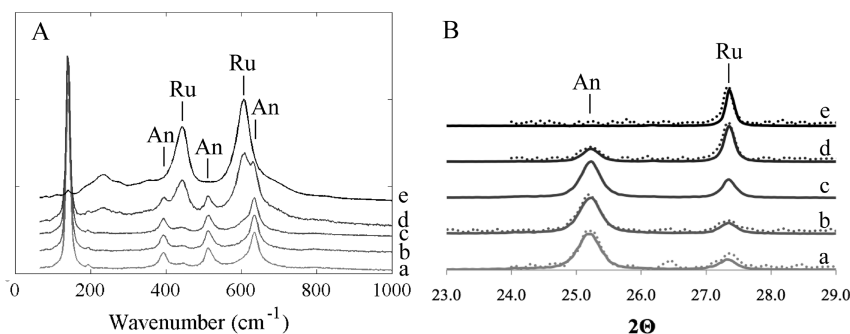


Figure 1. Raman (A) and XRD (B) spectra of photocatalysts calcined at 200 °C (a), 400 °C (b), 600 °C (c), 700 °C (d), and 800 °C (e). Peak positions of anatase and rutile are marked with “An” and “Ru”, respectively. Postreaction diffraction data are presented as dotted lines in the XRD data.

not comment on the effects of further increasing the oxidation temperature beyond 110 °C. In the limit of high temperature, charge carrier recombination dynamics should dramatically limit the number of charge carriers present on the photocatalyst surface. Knowledge from the solid state physics literature can be used in the analysis of such high-temperature recombination processes. Nonradiative, multiphonon recombination of photo-generated charge carriers become significant at photocatalyst temperatures equivalent to and larger than the Debye temperature of the photocatalyst ($\Theta_D = 327$ and 247 °C, for rutile and anatase TiO_2 , respectively).^{32,33,34} Up to now, the published research was limited to photocatalyst testing at temperatures too low to fully observe the effects of such recombination dynamics (e.g., $T < 110$ °C).

The purpose of this study is to investigate the high-temperature photocatalytic oxidation rates of ethylene over TiO_2 photocatalysts. Insights on the nonradiative, multiphonon recombination rates of charge carriers in TiO_2 photocatalysts can also be inferred from the analysis of high-temperature ethylene oxidation rate data. Ethylene was chosen as a probe VOC, because it is a parent molecule of other, more hazardous compounds, such as trichloroethylene. A unique photocatalytic reactor was constructed for this purpose, consisting of a very thin, flat catalyst bed (bed dimensions: 0.5 mm \times 30 mm \times 30 mm). The large area of the catalyst bed is illuminated on one side and heated from the opposing side. This configuration allows independent control of catalyst bed temperature and illumination of the catalyst bed according to the experimental conditions. Additional reactor details, such as CAD drawings and flow modeling results can be found in the Supporting Information.

EXPERIMENTAL SECTION

The TiO_2 photocatalyst (Degussa P25) was calcined at 200, 400, 600, 700, or 800 °C for 4 h in air to produce catalysts with a varied phase composition. These catalysts were then deposited on Davasil Silica Gel (35–60 mesh, Sigma-Aldrich #236802) that had been calcined at 800 °C in air for 4 h. The deposition procedure involved physical mixing of the calcined TiO_2 and SiO_2 (to achieve a 5 wt % $\text{TiO}_2/\text{SiO}_2$ loaded catalyst), followed by the submersion of the catalyst in deionized water and 20 min of ultrasonication. The mixed catalysts were then dried overnight in an oven at 120 °C. Characterization was conducted on the calcined, unsupported TiO_2 catalysts. Single-point BET surface areas were measured in a Quantachrome ChemBET-3000. Phase analysis of the anatase and rutile structures was calculated from XRD data, according to ref 5. Differential scanning calorimetry

(DSC) was conducted on a TA Q600 TGA/DSC to determine amorphous phase content.^{35–37} These experiments were conducted in an air environment at a heating rate of 40 °C/min. Diffuse reflectance UV/vis (DRUV/Vis) spectroscopy of each TiO_2 sample was acquired on a ThermoScientific Evolution 300 UV–visible spectrophotometer. The determination of surface hydroxyl concentration was conducted in a thermogravimetric analysis instrument (TA Q500) using ammonia desorption. A 1% NH_3 in N_2 gas stream was introduced to the dried catalyst for 60 min, followed by a 60 min purge with UHP N_2 , followed by a temperature programmed desorption ramp from 100 to 800 °C. The mass of desorbed ammonia was used as a measure of the surface hydroxyl concentration, using a 1:1 ratio of hydroxyl groups to adsorbed ammonia.

A model of the photocatalytic reactor used for oxidation experiments was designed in SolidWorks and tested for uniform temperature distributions and gas flow distributions across the catalyst bed using COMSOL Multiphysics simulations (Supporting Information, Figure 1A–C). The simulation demonstrated sufficient uniformity in both temperature and gas velocity profiles across the catalyst bed. The reactor was machined out of stainless steel and heated by 4 $\frac{1}{4}$ in. cartridge heaters, which were controlled by LabVIEW software. The illuminated side of the catalyst bed was sealed from the laboratory environment by a 1.0 cm thick section of GE 124 quartz (Technical Glass Products, 90% transmission at 365 nm). Quartz wool packing on the influent and effluent ends of the catalyst bed prevented channeling of the gas stream and immobilized the catalyst throughout the duration of the experiment. Figure 1D shows the flow reactor loaded with photocatalyst. UV illumination was achieved via a UV spot lamp (Blak-Ray B 100AP) located 10 cm from the catalyst bed. Intensity measurements taken under the quartz window showed that the catalyst bed received 25 mW/cm^2 of 365 nm illumination.

In a typical experiment, 125 mg of catalyst was loaded into the photocatalytic reactor, which was then sealed by the compression of a graphite gasket between the reactor body and the quartz window; a leak test was conducted to ensure a complete seal. The photocatalytic reactor was then wrapped in insulating glass wool, and the UV lamp positioned above the catalyst bed. Inlet gas consisted of 50 sccm dry air, 3 sccm ethylene (99.9%), and 50 sccm argon diluent. Gas flow rates and diluent concentrations were set to achieve minimal thermal ethylene conversion ($X_{\text{ethylene}} < 5\%$) at the highest temperatures studied. The reactant stream was then passed through a DI water saturator at room temperature before entering the photocatalytic reactor. External mass transfer

Table 1. Catalyst Characterization Results, Including Single-Point BET Surface Area, Surface Hydroxyl Concentrations ([OH]), Phase Analysis (by XRD and DSC), and Indirect Band Gap Estimates from DRUV/Vis Spectroscopies^a

calcination temperature (°C)	surface area (m ² g ⁻¹)	[OH] (μmol g ⁻¹)	phase content (wt%, amorphous/anatase/rutile)	band gap energy (eV)
200	52.2 (±0.6)	9.02 (±2.8)	10.6/65.4/24.0 (±6.2/4.5/1.7)	2.96
400	52.2 (±0.5)	6.62 (±3.0)	2.5/70.2/27.4 (±2.0/1.4/0.6)	2.96
600	45.4 (±0.6)	5.3 (±1.9)	0/60.6/39.4 (±0.5/0.6/0.7)	2.94
700	27.2 (±0.5)	5.0 (±2.2)	0/22.3/77.7 (±NA/0.6/0.7)	2.91
800	11.2 (±0.2)	4.0 (±2.9)	0/1.1/98.9 (±NA/0.6/0.7)	2.88

^a Standard measurement errors are reported in parentheses, where applicable.

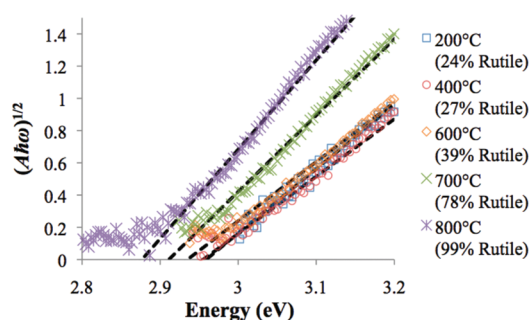


Figure 2. Determination of the indirect band transitions of calcined photocatalysts.

effects were negligible, as observed by independent rate measurements with respect to the square root of total flow rate over a range of space velocities a factor of 2 about the experimental flow rate.

A temperature program was built into the LabVIEW control software to ensure repeatability of experiments. The catalyst was first heated to 200 °C for 2 h to establish an acceptable equilibrium of gas phase components over the catalyst bed. The catalyst was then allowed to cool to 60 °C before starting the experiment. At each temperature step, oxidation rate data were acquired for 45 min with the UV lamp off, followed by 45 min with the UV lamp on. These rate data represent oxidation rates of the thermal process and the thermal plus photocatalytic process, respectively. The temperature steps during photocatalytic oxidation experiments were 60, 100, 170, 250, 325, 360, 400, 440, 480, and 520 °C, as measured in the center of the catalyst bed. Experiments with smaller temperature increments were introduced at higher temperatures to better discriminate photocatalytic oxidation rates from thermal oxidation rates, as the thermal oxidation rates become equivalent to or greater than the measured photocatalytic rates.

Oxidation rates were measured by quantifying effluent CO₂ concentrations via a Bruker Optics FTIR equipped with a gas flow cell. CO₂ concentrations were measured by the integration of the experimental CO₂ peak area (2400–2300 cm⁻¹) and calibrated to the CO₂ peak area of a 500 ppm CO₂ standard. The CO₂ peak area calibration curve was found to be linear with respect to CO₂ concentration across the experimentally observed range of CO₂ concentrations.

A diffuse reflectance infrared spectrometer (DRIFTS) accessory was used in the Bruker Optics FTIR to assess the presence of surface hydroxyl species before and after high temperature photocatalytic oxidation reactions. In this experiment, a 1 wt % TiO₂/KBr sample (600 °C TiO₂ calcination temperature) was loaded into the DRIFTS cell and heated to 200 °C for 30 min in

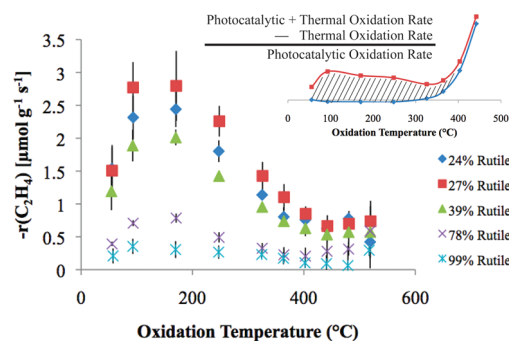


Figure 3. Experimental photocatalytic oxidation data for all five TiO₂ catalysts. The inset shows the calculation of photocatalytic oxidation rates from raw experimental data.

dry nitrogen to remove physically adsorbed water. The sample was then cooled to 20 °C in dry nitrogen and a DRIFTS spectrum of the dry TiO₂ catalyst was recorded at 2 cm⁻¹ resolution with 512 scans. The DRIFTS-mounted sample was then exposed to the reactant gas stream (C₂H₄, O₂, H₂O, and Ar), UV illumination, and 600 °C catalyst bed temperature for 1 h. After 1 h duration, the reactant gas was replaced by dry nitrogen, and the bed temperature was lowered to 200 °C for 30 min to remove water from the catalyst bed. A final spectrum was taken once the sample had cooled to 20 °C under dry nitrogen.

RESULTS

Single-point BET surface area measurements of each calcined TiO₂ photocatalyst (Table 1) gave values similar to those reported in literature. Surface hydroxyl concentrations and XRD phase analysis results are also presented in Table 1, while the Raman and XRD spectra are shown in Figure 1. Amorphous, anatase, and rutile phase compositions were calculated from XRD and DSC data. Amorphous to anatase phase transitions were observed between 388 and 400 °C for samples calcined to 200 and 400 °C, while no transition was observed for samples calcined at higher temperatures; these results are consistent with previously reported phase transition behavior.^{35–37} The rutile and amorphous TiO₂ phase compositions were strongly dependent on calcination temperature. DRUV/Vis spectroscopy confirmed that the band gap energies for each sample followed the expected trends: DRUV/Vis results are shown in Figure 2, while band gap energies are shown in Table 1.

Experimental data for the photocatalytic oxidation of ethylene are presented in Figure 3. The inset of Figure 3 illustrates the calculation of the photocatalytic oxidation rate; the oxidation rate in the absence of UV illumination was subtracted from the oxidation rate during UV illumination at each experimental oxidation

temperature. It should be noted that two of the five catalysts, namely the 200 and 400 °C calcined catalysts, were tested for photocatalytic oxidation at temperatures exceeding their respective calcination temperatures. In an effort to extract useful information from oxidation results of these catalysts, phase analysis was conducted on the postreaction XRD patterns for every catalyst. The pre- and postreaction phase composition results are used as the bounds for error bars on the averaged phase composition for all data discussed in the following sections.

All catalysts exhibited an exponential increase in thermally oxidized ethylene with increased reaction temperature. The addition of UV photons contributed to ethylene conversion at low and moderate temperatures ($T < 325$ °C); however, as the temperature increased, the presence of UV photons had a diminished effect. As shown in Figure 3, the photocatalytic oxidation rates reached a maximum between 100 and 200 °C and decreased to near-zero values at 500 °C.

The presence of surface hydroxyl groups after reaction was confirmed by the independent DRIFTS experiment. Figure 2 in the Supporting Information shows the OH-stretching region of the acquired spectra; the native TiO₂ hydroxyl groups remained after 1 h of photocatalytic oxidation at 600 °C.

DISCUSSION

Maximum photocatalytic ethylene oxidation rates were observed between 100 and 200 °C for all catalysts tested. To exactly pinpoint the temperature for maximum oxidation rates would require additional experiments with smaller temperature increments; however, the observations made with the current set of temperatures are sufficient to confirm that the maximum oxidation rate occurs above the previously reported temperature range of 60–110 °C. The observed trend of increased oxidation rates at temperatures less than 200 °C were due to differences in ethylene and water adsorption energies on the polar Ti–OH surface;²⁹ increased oxidation temperature shifts the adsorbate concentrations closer to stoichiometric ratios, thereby increasing ethylene oxidation rates.

The loss of photocatalytic activity at high temperatures can be attributed to the loss of either of two photocatalytic intermediate species: surface hydroxyl groups or photogenerated charge carriers. Photogenerated charge carriers and surface-bound hydroxyl groups are directly involved in the oxidation mechanism.^{12,23,28} The results of the DRIFTS experiment show that surface hydroxyl groups persist on the TiO₂ catalyst after 60 min of photocatalytic oxidation at high temperature and ethylene conversion (Supporting Information, Figure 2). Therefore, the decreasing photocatalytic activity above 200 °C must be due to the loss of photogenerated charge carriers.

The loss of photogenerated charge carriers can take place through multiple routes; the most relevant recombination pathways include radiative and nonradiative recombination. PL emission spectroscopy, for example, measures the energy of emitted photons from the radiative recombination of photogenerated charge carriers. In nonradiative recombination, inelastic collisions between charge carriers and phonons result in lost charge carrier energy. Nonradiative interactions typically involve multiple phonon participation in large band gap materials and occur with increasing probability as temperatures increase, due to the increase in the population of high-energy phonons and in the interphonon interaction rates (most notably the three-phonon interactions). Nonradiative, multiphonon recombination pathways

have been well-characterized for lasing materials, such as doped Ti³⁺:Al₂O₃ and Yb³⁺:Y₂O₃,³³ as well as in other luminescence-based chemistries.³⁸

The temperature dependence of both recombination pathways are of particular interest to the current investigation: the rate of radiative recombination (γ_{rad}) is independent of temperature, while the rate of nonradiative recombination (γ_{nonrad}) is dependent on temperature³⁹ and is shown in eq 1.³⁴

$$\gamma_{\text{nonrad}} = \gamma_{\text{rad}(T=0\text{K})} (1 - e^{-\hbar\omega_p/k_B T})^{-N_p} \quad (1)$$

Here, the average phonon energy is represented by $\hbar\omega_p$, while N_p represents the number of phonons participating in recombination. The prefactor, $\gamma_{\text{rad}(T=0\text{K})}$, is the radiative recombination rate at 0 K, due to the lack of phonons and nonradiative recombination at 0 K. Equation 1 assumes the nonradiative recombination is controlled by the equilibrium occupancy of a phonon with this energy, and not by its rate of conversion (up or down) toward equilibrium.⁴⁰

Equation 1 can be used to derive a modified oxidation rate equation, based on fundamental knowledge of photocatalytic rate equations. For instance, a hallmark feature of a photocatalytic rate law is the dependence of rate on the illumination intensity (I) and the quantum efficiency (ϕ). Quantum efficiency is the ratio of radiative decay rate to the sum of radiative and nonradiative decay rates and is usually calculated as ratio of the rate of moles of product formed (γ_{products}) to the rate of moles of sufficiently energetic incident photons, which is proportional to the rate of charge carrier generation ($\gamma_{e^-/h^+ \text{ formation}}$), as in eq 2.

$$\phi \propto \frac{\gamma_{\text{products}}}{\gamma_{e^-/h^+ \text{ formation}}} \quad (2)$$

Under steady state illumination, the accumulation of charge carriers should be negligible (eq 3). Therefore, the rate of recombination of charge carriers (γ_{recomb}) should equal the rate of generation of charge carriers, i.e.,

$$\frac{d(e^-/h^+)}{dt} = 0 = \gamma_{e^-/h^+ \text{ formation}} - \gamma_{\text{recomb}} \quad (3)$$

Three charge carrier recombination pathways are relevant at the temperatures investigated here: radiative recombination (γ_{rad}), nonradiative recombination (γ_{nonrad}), and charge transfer to intermediate species with the final result of product formation (eq 4), i.e.,

$$\gamma_{\text{recomb}} = \gamma_{\text{rad}} + \gamma_{\text{nonrad}} + \gamma_{\text{products}} \quad (4)$$

Given eqs 2–4, the quantum efficiency can be rewritten as in eq 5.

$$\phi \propto \frac{\gamma_{\text{products}}}{\gamma_{e^-/h^+ \text{ formation}}} = \frac{\gamma_{\text{products}}}{\gamma_{\text{rad}} + \gamma_{\text{nonrad}} + \gamma_{\text{products}}} \quad (5)$$

Due to the high occupancy of the high energy phonons emitted in the multiphonon emission at elevated temperatures ($\gamma_{\text{nonrad}} \gg \gamma_{\text{rad}} + \gamma_{\text{chem}}$),³⁴ the quantum efficiency can be simplified and combined with eq 1 to reflect temperature effects on quantum efficiency (eqs 6 and 7) and we have

$$\phi \propto \frac{\gamma_{\text{products}}}{\gamma_{\text{nonrad}}} = \frac{\gamma_{\text{products}}}{\gamma_{\text{rad}(T=0\text{K})}} (1 - e^{-\hbar\omega_p/k_B T})^{-N_p} \quad (6)$$

$$\phi = k_{\phi} (1 - e^{-\hbar\omega_p/k_B T})^{-N_p} \quad (7)$$

Table 2. Regressed Parameters from the Four-Parameter Ethylene Photocatalytic Oxidation Rate Equation (eq 9)^a

calcination temperature (°C)	$k_{app,\phi}$ ($\mu\text{mol g}^{-1} \text{s}^{-1}$)	E_{app} (kJ mol^{-1})	$\hbar\omega_p$ (meV)	N_p	r^2
200	136.8 (130.1, 143.5)	12.13	94.9 (93.8, 96.0)	17	0.94
400	141.0 (133.6, 148.3)	12.13	100.2 (99.0, 101.5)	18	0.93
600	104.0 (99.0, 108.9)	12.13	98.9 (97.9, 100.0)	18	0.94
700	41.2 (37.6, 44.7)	12.13	96.3 (94.3, 98.3)	18	0.88
800	17.6 (16.5, 18.6)	12.13	98.0 (96.6, 99.3)	17	0.91

^a Standard error estimates from the regression are presented in parentheses.

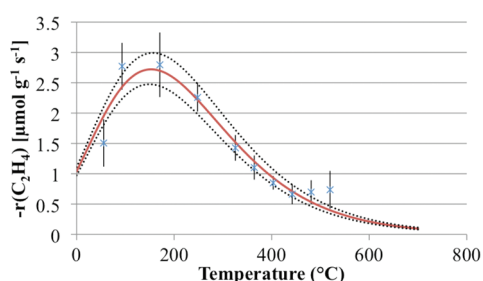


Figure 4. Results from nonlinear regression of eq 9 on experimental photocatalytic oxidation data for the catalyst calcined at 400 °C (Figure 3 in the Supporting Information shows similar data for all five catalysts). Solid lines represent the regressed model, while dotted lines represent the regressed model with standard error estimates of the fitted parameters.

where k_ϕ is the temperature-independent quantum efficiency term. Therefore, introduction of the temperature-dependent quantum efficiency term (eq 7) into a generic photocatalytic ethylene oxidation rate equation produces eq 8,

$$-r_{\text{C}_2\text{H}_4} = k_{app} P_{\text{C}_2\text{H}_4}^\alpha P_{\text{O}_2}^\beta P_{\text{H}_2\text{O}}^\delta I (k_\phi (1 - e^{-\hbar\omega_p/k_B T})^{-N_p}) \quad (8)$$

In eq 8, k_{app} is the apparent rate constant and the partial pressures of reactants and products are represented. This rate equation simplifies to a four-term model if the partial pressures of reactants and products are held constant for each experiment at different temperatures. The total ethylene conversion was limited below 5% at 520 °C oxidation temperature, therefore, the simplified photocatalytic oxidation model is shown in eq 9 using an apparent activation energy E_{app} and a combined pre-exponential term, i.e.,

$$-r_{\text{C}_2\text{H}_4} = k_{app,\phi} e^{-E_{app}/RT} (1 - e^{-\hbar\omega_p/k_B T})^{-N_p} \quad (9)$$

We note that the phonon participation is only represented through the occupancy of energy $\hbar\omega_p$ and the kinetics of interphonon interactions that include the density of states (or the Debye temperature under assumption of no dispersion) are not considered. A complete treatment should apply the Fermi golden rule as for example in ref 40. We also note that instead of the bulk phonons on the TiO_2 substrate, we should consider surface phonons that couple with the frustrated motion of the adsorbates. So, we expect eq 9 to be a rough first approximation of the process.

Nonlinear regression was performed in MATLAB using the “nlinfit” tool. A poor fit was obtained for the regression of the four-parameter model to the experimental data. Therefore, it was necessary to reduce the number of model parameters. The apparent

activation energy for ethylene photocatalytic oxidation is generally agreed to be approximately 3.0 kcal/mol (12.13 kJ/mol).^{22,25,26} Therefore, this parameter was fixed. The three-parameter nonlinear regression produced acceptable results; the regressed parameters and their standard error estimates are shown in Table 2 along with the r^2 values for each fit. Results from the regression are plotted with experimental data in Figure 4 and in Figure 3 of the Supporting Information.

The modeled rate equation (eq 9) effectively separates rate effects due to chemical kinetic limitations and charge carrier limitations. Analysis of the regressed model parameters reveal information about the temperature-dependent and -independent terms for a range of TiO_2 phase compositions. For instance, the pre-exponential factor, $k_{app,\phi}$, represents the lumped temperature-independent terms of the kinetic apparent pre-exponential factor, reactant and product partial pressures, temperature-independent quantum efficiency, and illumination intensity. Pressure terms and illumination intensity terms were assumed to be independent of catalyst phase. Therefore, the regressed pre-exponential factor for each catalyst reflects changes in the kinetic apparent pre-exponential factor and/or the temperature independent quantum efficiency term. Figure 5A shows the regressed pre-exponential factor as a function of the measured catalyst rutile phase. The product of the kinetic apparent pre-exponential term with the temperature-independent quantum efficiency term results in an observed linear trend with respect to catalyst phase. In addition, the use of the measured surface hydroxyl species concentration as a normalization parameter produced regressed parameters that were also phase dependent (Figure 5B). These observations agree with previous observations of phase-dependent photocatalytic activity of TiO_2 .^{8–11}

Information regarding charge carrier recombination dynamics can also be gleaned from analysis of the regressed phonon energy ($\hbar\omega_p$) and phonon number (N_p) parameters. The density of phonon density of states for both anatase and rutile TiO_2 were calculated and reported in ref 41; depending on the calculation method used, the maximum phonon energies are 810–875 cm^{-1} (100–109 meV) and 780–825 cm^{-1} (97–102 meV), respectively.⁴¹ The regressed phonon energy values, shown in Table 2, are approximately 10–20 meV below the predicted maximum phonon energies for TiO_2 . The standard error on the regression parameters reveals insignificant correlation of phonon energy to phase composition, which was expected, given the close relation of phonon density of states between rutile and anatase phases of TiO_2 . Additionally, the regressed parameter for the number of phonons participating in charge carrier decay, N_p , range between 17 and 18, at or below, i.e., the accepted maximum of 18 phonons.⁴²

A common correlation between the phonon energy and number of participating phonons in nonradiative, multiphonon

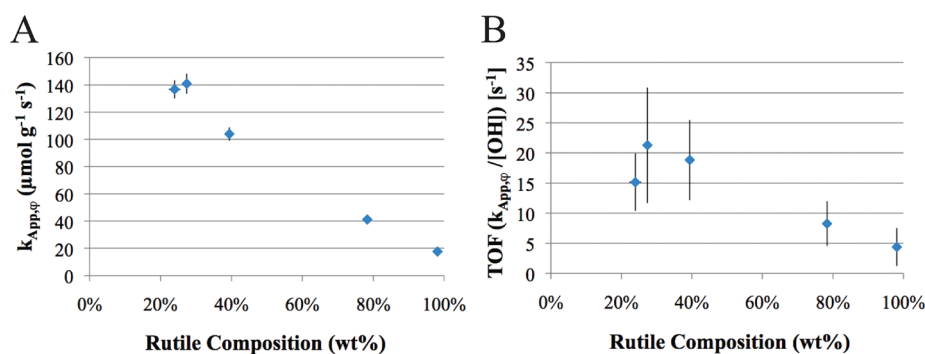


Figure 5. Fitted pre-exponential factors (A) for each catalyst, plotted as a function of the rutile phase content in each catalyst. The pre-exponential factors have been reported as a function of the catalyst mass. Turnover frequency (B), calculated from the normalization of the regressed pre-exponential factor (A) with the measured surface hydroxyl concentration (mol g^{-1}) determined from NH_3 -desorption experiments.

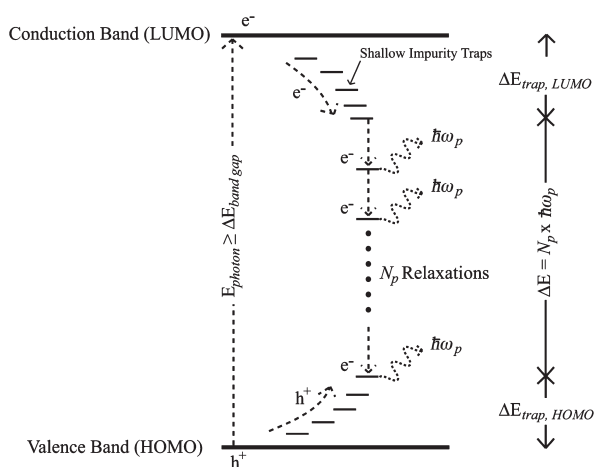


Figure 6. Diagram of photon absorption and charge formation and the charge carrier relaxation (recombination) processes, showing the traditional band gap energy, trap and defect energy levels, and the multiphonon relaxation process which takes place with increased probability at higher temperatures.

recombination processes is the energy gap law (EGL). The EGL states that the product of the phonon energy with the number of phonons is equal to the dissipated charge carrier energy.⁴³ The total energy dissipated due to nonradiative decay will be referred to as the EGL dissipation energy; the EGL dissipation energy for each of the photocatalysts tested varies between 1.60 and 1.80 eV. The difference in energy between the TiO_2 band gap, measured by DRUV/Vis, and the EGL dissipation energy can be attributed to energy loss of the charge carrier due to defects and trap states present in the photocatalyst. Electronic trap states are common, especially in mixed phase solids, such as P25.³ While many of these trap states occupy energy levels hundreds of millielectronvolts below the conduction band, some have been reported as low as 1.5 eV below the conduction band of anatase TiO_2 .⁴⁴ A schematic of the combined decay processes is presented in Figure 6. This schematic illustrates photogenerated electron transfer from the conduction band to lower energy trap states. At elevated temperatures, the electron can undergo nonradiative, multiphonon decay into hole trap states, which lie slightly above the valence band. Although the nonradiative decay occurs instantaneously and emits N_p phonons, the process is shown piecewise in Figure 6 for simplicity.

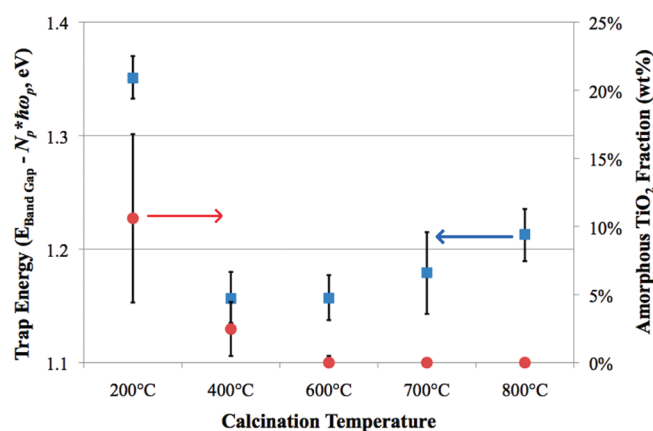


Figure 7. Energy lost to trap states, calculated from the subtraction of the energy lost via multiphonon recombination (via the energy gap law) from the measured band gap energy and the measured amorphous TiO_2 phase content, measured via DSC. Each promoted electron contains an energy equivalent to the band gap energy; however, the energy gap law can only account for a fraction of the nonradiative recombination energy. The difference in recombination energy can be attributed to the energy of recombination lost to charge carrier decay to trap and impurity states.

The trap energy ($E_{\text{trap}} = E_{\text{band gap}} - E_{\text{EGL dissipation}}$) for the five catalyst calcination temperatures is shown in Figure 7. The catalyst calcined at 200 °C exhibits the largest band gap energy and the lowest EGL dissipation energy, and therefore the largest trap energy. The 200 °C calcination sample also exhibited the maximum content of amorphous TiO_2 , as determined by DSC measurements. This suggested that the 200 °C calcined catalyst contained significantly deeper-lying trap states than the other catalysts. Further, calcination to 400 °C removes these trap sites or impurities without dramatically changing the observed band gap energy (Table 1). Therefore, the presence of heavy trap states in the 200 °C calcined sample is most likely due to the presence of amorphous TiO_2 , which may be removed by heat treatment above the amorphous-to-anatase phase transition, at approximately 400 °C.

Extension of this analysis can be used to guide the development of photocatalysts designed to operate more efficiently at elevated temperatures. For example, current VOC oxidation photocatalysts have been shown to operate with a maximum photocatalytic rate between 60 and 200 °C [this work and refs 25

and 28–31]. Equation 9 predicts that Degussa P25 operating between 60 and 200 °C has an effective quantum efficiency of approximately 25–60% of its maximum quantum efficiency, due to nonradiative, multiphonon recombination dynamics. Given a wide range of tunable variables, such as band gap energies, trap, vacancy or impurity states, and phonon dispersion characteristics, high-temperature photocatalysts could be designed to be less affected by nonradiative recombination limitations, thus improving elevated temperature photocatalytic operating efficiencies.

CONCLUSIONS

The aim of this work was to understand fundamental limitations of high-temperature photocatalytic reactions using the photocatalytic oxidation of ethylene as a probe reaction. A novel high-temperature photocatalytic reactor was designed and constructed to achieve high catalyst bed temperatures while maximizing the illuminated photocatalyst bed area. The photocatalyst tested was a heat-treated Degussa P25 TiO₂, which contained different anatase and rutile phase compositions than the commercially available powder. Photocatalytic oxidation experiments showed that the photocatalyst achieved significant oxidation rates at catalyst bed temperatures of up to 350 °C. The maximum photocatalytic oxidation rate was observed between 100 and 200 °C; higher photocatalyst temperatures resulted in a decreased oxidation rate. The decline in photocatalytic activity can be attributed to the nonradiative, multiphonon recombination of charge carriers, which was modeled by an exponential function of temperature and two bulk TiO₂ properties: phonon energy and phonon participation number. Further, the fitted model parameters from the nonlinear regression analysis are physically reasonable and can be used to simultaneously extract information regarding temperature independent photocatalytic activity and electronic trap states of the photocatalyst. Using this information, photocatalysts designed with specific phonon energy, phonon number, band gap energy, and trap states could be engineered with decreased high-temperature charge-carrier recombination rates. This could lead to catalysts with increased photocatalytic VOC oxidation efficiencies at elevated temperatures.

ASSOCIATED CONTENT

S Supporting Information. Additional figures that describe the photocatalytic reactor used in these experiments, as well as experimental photocatalytic oxidation data and regression results. This material is available free of charge via the Internet at <http://pubs.acs.org>.

REFERENCES

- (1) Carneiro, J. T.; Savenije, T. J.; Moulin, J. A.; Mul, G. *J. Phys. Chem. C* **2010**, *114*, 327–332.
- (2) Hurum, D. C.; Gray, K. A.; Rajh, T.; Thurnauer, M. C. *J. Phys. Chem. B* **2005**, *109*, 977–980.
- (3) Knorr, F. J.; Mercado, C. C.; McHale, J. L. *J. Phys. Chem. C* **2008**, *112*, 12786–12794.
- (4) Nakajima, H.; Mori, T.; Shen, Q.; Toyoda, T. *Chem. Phys. Lett.* **2005**, *409*, 81–84.
- (5) Porter, J. F.; Yu-Guang, L.; Chan, C. K. *J. Mater. Sci.* **1999**, *34*, 1523–1531.
- (6) Park, D. R.; Zhang, J.; Ikeue, K.; Yamashita, H.; Anpo, M. *J. Catal.* **1999**, *185*, 114–119.
- (7) Hurum, D. C.; Agrios, A. G.; Gray, K. A.; Rajh, T.; Thurnauer, M. C. *J. Phys. Chem. B* **2003**, *107*, 4545–4549.
- (8) Choi, W.; Termin, A.; Hoffmann, M. R. *J. Phys. Chem.* **1994**, *98*, 13669–13679.
- (9) Ohno, T.; Tokieda, K.; Higashida, S.; Matsumura, M. *Appl. Catal. A* **2003**, *244*, 383–391.
- (10) Kawahara, T.; Konishi, Y.; Tada, H.; Tohge, N.; Nishii, J.; Ito, S. *Angew. Chem., Int. Ed.* **2002**, *41*, 2811–2813.
- (11) Wu, C.; Yue, Y.; Deng, X.; Hua, W.; Gao, Z. *Catal. Today* **2004**, *93–95*, 863–869.
- (12) Fox, M. A.; Dulay, M. T. *Chem. Rev.* **1993**, *93*, 341–357.
- (13) Linesbigger, A. L.; Lu, G.; Yates, J. T. *Chem. Rev.* **1995**, *95*, 735–758.
- (14) Ni, M.; Leung, M. K.; Leung, D. Y.; Sumathy, K. *Renewable Sustainable Energy Rev.* **2007**, *11*, 401–425.
- (15) Mills, A.; Hunte, S. L. *J. Photochem. Photobiol. A* **1997**, *108*, 1–35.
- (16) Cowan, A. J.; Tang, J.; Leng, W.; Durrant, J. R.; Klug, D. R. *J. Phys. Chem. C* **2010**, *114*, 4208–4214.
- (17) Wold, A. *Chem. Mater.* **1993**, *5*, 280–283.
- (18) Arabatzis, I. M.; Stergiopoulos, T.; Bernard, M. C.; Labou, D.; Neophytides, S. G.; Faralas, P. *Appl. Catal., B* **2003**, *42*, 187–201.
- (19) Jung, K. Y.; Park, S. B.; Ihm, S. K. *Appl. Catal., A* **2002**, *224*, 229–237.
- (20) Maira, A. J.; Yeung, K. L.; Lee, C. Y.; Yue, P. L.; Chan, C. K. *J. Catal.* **2000**, *192*, 185–196.
- (21) Houas, A.; Lachheb, H.; Ksibi, M.; Elaloui, E.; Guillard, C.; Herrmann, J. M. *Appl. Catal., B* **2001**, *31*, 145–157.
- (22) Ohko, Y.; Hasimoto, K.; Fujishima, A. *J. Phys. Chem. A* **1997**, *101*, 8057–8062.
- (23) Fujishima, A.; Zhang, X.; Tryk, D. A. *Surf. Sci. Rep.* **2008**, *63*, 515–582.
- (24) Chong, M. N.; Jin, B.; Chow, C. W.; Saint, C. *Water Res.* **2010**, *44*, 2997–3027.
- (25) Obee, T. N.; Hay, S. T. *Environ. Sci. Technol.* **1997**, *31*, 2034–2038.
- (26) Brigden, C. T.; Poulston, S.; Twigg, M. V.; Walker, A. P.; Wilkins, A. J. *Appl. Catal., B* **2001**, *32*, 63–71.
- (27) Vorontsov, A. V.; Savinov, E. N.; Kurkin, E. N.; Torbova, O. D.; Parmon, V. N. *React. Kinet. Catal. Lett.* **1997**, *62*, 83–88.
- (28) Yamazaki, S.; Tanaka, S.; Tsukamoto, H. *J. Photochem. Photobiol. A* **1999**, *121*, 55–61.
- (29) Fu, X.; Clark, L. A.; Zeltner, W. A.; Anderson, M. A. *J. Photochem. Photobiol. A* **1996**, *97*, 181–186.
- (30) Tibbitts, T. W.; Cushman, K. E.; Fu, X.; Anderson, M. A.; Bula, R. J. *Adv. Space Res.* **1998**, *22*, 1443–1451.
- (31) Sirisuk, A.; Hill, C. G.; Anderson, M. A. *Catal. Today* **1999**, *54*, 159–164.
- (32) Howard, C.; Sabine, T.; Dickson, F. *Acta Crystallogr.* **1991**, *B47*, 462–468.
- (33) Powell, R. C. *Physics of Solid-State Laser Materials*; Springer-Verlag Inc.: New York, 1998.
- (34) Kaviany, M. *Heat Transfer Physics*; Cambridge University Press: Cambridge, U.K., 2008.
- (35) Ohtani, B.; Ogawa, Y.; Nishimoto, S. *J. Phys. Chem. B* **1997**, *101*, 3746–3752.
- (36) Svadlak, D.; Shanelova, J.; Malek, J.; Perez-Maqueda, L.; Criado, J.; Mitsushashi, T. *Thermochim. Acta* **2004**, *414*, 137–143.
- (37) Xie, H.; Zhang, Q.; Xi, T.; Wang, J.; Liu, Y. *Thermochim. Acta* **2002**, *381*, 45–48.
- (38) Basiev, T.; Dergachev, A.; Orlovskii, Y.; Prokhorov, A. *J. Lumin.* **1992**, *53*, 19–23.
- (39) Layne, C.; Lowdermilk, W.; Weber, M. *Phys. Rev. B* **1977**, *16*, 10–20.
- (40) Kim, J.; Kaviany, M. *J. Appl. Phys.* **2011** submitted for publication.
- (41) Shojae, E.; Mohammadzadeh, M. R. *J. Phys.: Condens. Matter* **2010**, *22*, 015401.
- (42) Ohsaka, T.; Izumi, F.; Fujiki, Y. *J. Raman Spectrosc.* **1978**, *7*, 321–324.
- (43) Englman, R.; Jortner, J. *Mol. Phys.* **1970**, *18*, 145–164.
- (44) Wang, X.; Feng, Z.; Shi, J.; Jia, G.; Shen, S.; Zhou, J.; Li, C. *Phys. Chem. Chem. Phys.* **2010**, *12*, 7083–7090.